Science Bulletin 68 (2023) 1886–1893

Contents lists available at ScienceDirect

Science Bulletin

journal homepage: www.elsevier.com/locate/scib

Article

Bioinspired microenvironment modulation of metal–organic framework-based catalysts for selective methane oxidation

Jianfei Sui [a], Ming-Liang Gao [a], Bing Qian [b], Chengyuan Liu [b], Yang Pan [b], Zheng Meng [a,*], Daqiang Yuan [c], Hai-Long Jiang [a,*]

[a] Department of Chemistry, University of Science and Technology of China, Hefei 230026, China
[b] National Synchrotron Radiation Laboratory (NSRL), University of Science and Technology of China, Hefei 230029, China
[c] State Key Laboratory of Structural Chemistry, Fujian Institute of Research on the Structure of Matter, Chinese Academy of Sciences, Fuzhou 350002, China

ARTICLE INFO

Article history:
Received 8 May 2023
Received in revised form 21 June 2023
Accepted 7 July 2023
Available online 24 July 2023

Keywords:
Methane oxidation
Microenvironment modulation
Metal–organic frameworks
Bioinspired
Catalysis

ABSTRACT

Inspiration from natural enzymes enabling creationary catalyst design is appealing yet remains extremely challenging for selective methane (CH_4) oxidation. This study presents the construction of a biomimetic catalyst platform for CH_4 oxidation, which is constructed by incorporating Fe-porphyrin into a robust metal–organic framework, UiO-66, furnished with saturated monocarboxylic fatty acid bearing different long alkyl chains. The catalysts demonstrate the high efficiency in the CH_4 to methanol (CH_3OH) conversion at 50 °C. Moreover, the selectivity to CH_3OH can be effectively regulated and promoted through a fine-tuned microenvironment by hydrophobic modification around the Fe-porphyrin. The long-chain fatty acids anchored on the Zr-oxo cluster of UiO-66 can not only tune the electronic state of the Fe sites to improve CH_4 adsorption, but also restrict the amount of H_2O_2 around the Fe sites to reduce the overoxidation. This behavior resembles the microenvironment regulation in methane monooxygenase, resulting in high CH_3OH selectivity.

1. Introduction

Selective conversion of CH_4 to CH_3OH, recognized as the "Holy Grail" reaction, is an exceptionally attractive approach for the production of high-value organic products. However, catalytically promoting this conversion under mild conditions remains a formidable challenge due to the high energy barrier (104 kcal mol^{-1}) for the C–H bond activation in CH_4 and the inevitable occurrence of overoxidation reactions [1–6]. In nature, certain organisms like methanotrophic bacteria are capable of converting CH_4 to CH_3OH using O_2 under ambient conditions, thanks to methane monooxygenases (MMOs) [7,8]. MMOs often feature intricate subcomponents that synergistically perform diverse tasks during CH_4 oxidation, such as the transport and binding of substrate molecules and the positioning of active sites, ultimately leading to exceptional activity and selectivity to CH_3OH. As an illustrative example, the soluble methane monooxygenase (sMMO) has three constituent components, the hydroxylase, the β unit, and the reductase, each of which is essential for efficient CH_4 to CH_3OH conversion. The iron sites in the active component hydroxylase alter their electronic state through the binding to the regulatory component β unit and are activated by the reductase, initiating CH_4 hydroxylation [9–11]. The β unit can change the volume and hydrophobicity of the active site cavity of the hydroxylase. This modification not only creates space but also increases the affinity for hydrophobic substrate molecules (e.g., CH_4) [8,12–14]. The coordinated interaction of these components necessitates the precise control of chemical microenvironments of the active site in MMOs for efficient and selective conversion of CH_4 to CH_3OH [15,16].

Drawing inspiration from natural MMOs, many catalytic systems, including iron and copper-based coordination complexes that aim to achieve the selective conversion of CH_4 to CH_3OH through a biomimetic way, have been developed [8]. The structure of active sites in these molecular catalysts usually can be readily designed with high fidelity to those found in MMOs; however, their performance in the reaction remains unsatisfactory [17–19]. Furthermore, molecular catalysts usually encounter challenges with recyclability and stability, which lead to decreased activity. To achieve efficient conversion of CH_4 to CH_3OH, it is highly desirable to develop catalysts that simultaneously possess active site analogs of MMOs and a suitable chemical microenvironment

* Corresponding authors.
E-mail addresses: zhengmeng@ustc.edu.cn (Z. Meng), jianglab@ustc.edu.cn (H.-L. Jiang).

https://doi.org/10.1016/j.scib.2023.07.031
2095-9273/

around active sites. However, the creation of corresponding microenvironment around MMOs active sites is very challenging due to the lack of sufficient tunability and complexity in common porous solids [20–22].

As a relatively new class of crystalline solids, metal–organic frameworks (MOFs) [23–30] are widely acknowledged as an appropriate platform for mimicking enzymes, because of their functionalization capability for introducing various active sites and tunable chemical structures with atomic precision [31–35]. Biomimetic catalysts utilizing MOFs as platforms has been implemented by either incorporating basic constituents featuring similar functionalities as enzymes or encapsulating synthetic active-site analogs into the scaffolds of MOFs [32,33]. Despite the encouraging progress, biomimetic catalysts that take full advantage of the structural features of MOFs for tuning the microenvironment for catalytic conversion of CH_4 to CH_3OH are still lacking [32]. Our vision is to leverage the highly customizable structure of MOFs to purposefully create precise and collaborative microenvironments. These microenvironments can facilitate the accumulation of substrate molecules, offer transmission channels, and create a confined hydrophobic pocket around the active site—reminiscent of those in the natural MMOs—to offer optimal catalytic performance.

In this study, we incorporated Fe-TCPP (TCPP = tetrakis(4-carboxyphenyl)porphyrin) into a robust MOF, namely UiO-66, which is further furnished by using saturated monocarboxylic fatty acid with different long alkane chains (C_n, n = 12, 14, 16, and 18). Although Fe-TCPP does not have exactly the same structure with the active component of monooxygenase cytochrome P450, they both share an iron porphyrin fragment, making Fe-TCPP (a suitable analog for P450) an active-site [36,37]. The resulting Fe^{3+}@UiO-66-C_n, featuring Fe-TCPP catalytic sites with a hydrophobic microenvironment created by the fatty acids (Scheme 1), achieve efficient and selective conversion of CH_4 to CH_3OH under mild conditions. Interestingly, the hydrophobic modification around Fe-TCPP with fatty acids bearing long alkane chains significantly enhances and tunes the selectivity towards CH_3OH in CH_4 oxidation. This hydrophobic modification not only regulates the electron state of the Fe active sites, but also tunes the concentration of reactive oxygen species around Fe sites, mimicking the microenvironment regulation mechanism observed in sMMO. To the best of our knowledge, this study represents the first report on MOF composites that mimick the microenvironment modulation in sMMO enzyme-like system for the selective conversion of CH_4 to CH_3OH.

2. Materials and methods

2.1. Synthesis of UiO-66

The UiO-66 was synthesized following a previously reported procedure with minor modifications [38]. In a typical process, 0.16 mmol $ZrCl_4$ (37.2 mg), 0.16 mmol 1,4-benzenedicarboxylic acid (BDC, 29 mg), 1.2 mL acetic acid, and 10 mL *N,N*-dimethylformamide (DMF) were dissolved in a 25 mL glass vial by ultrasonication treatment for 5 min, then the vial was sealed and placed in an oven at 120 °C for 24 h. The resulting powder was collected by centrifugation, washed with DMF and acetone, immersed in acetone for 3 d to remove residual DMF, and finally dried in a vacuum at 60 °C prior to use.

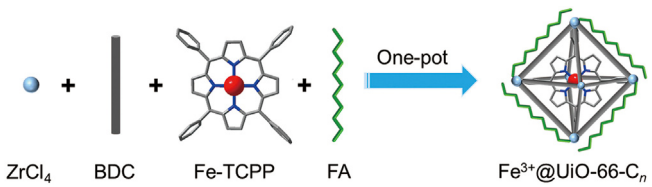

Scheme 1. (Color online) Schematic illustration showing the synthetic process for Fe^{3+}@UiO-66-C_n (n = 12, 14, 16, and 18).

2.2. Synthesis of Fe^{3+}@UiO-66-C_n (n = 12, 14, 16, and 18)

In a typical process, 0.343 mmol $ZrCl_4$ (80 mg) and 12 mmol monocarboxylic long-chain saturated fatty acids (2.40 g lauric acid, 2.74 g myristic acid, 3.08 g palmitic acid, or 3.41 g octadecanoic acid) and 20 mL of DMF were dissolved in a 25 mL glass vial by ultrasonication for 30 min, Then, 0.343 mmol BDC (57.0 mg) and 10.0 mg Fe-TCPP were added in the glass vial and the vial was sealed and placed in an oven at 130 °C for 24 h. The resulting powder was collected by centrifugation, washed with DMF and acetone, and immersed in acetone for 3 d to remove DMF, and then dried in vacuum at 60 °C before use.

3. Results and discussion

3.1. Synthesis and characterization

Fe^{3+}@UiO-66-C_n composites were synthesized by reacting $ZrCl_4$, Fe-TCPP, and BDC in DMF in the presence of long-chain saturated fatty acids with different chain lengths. All obtained products are UiO-66-based with good phase purity. No PCN-222 or PCN-224 phase which forms through self-nucleation between Zr^{4+} and Fe-TCPP in these catalysts can be found, as suggested by the powder X-ray diffraction (XRD) patterns (Figs. S1, S2 online). Despite that the size of the tetrahedron and octahedron cage of UiO-66 is smaller than the line length of Fe-TCPP, Fe-TCPP can still be incorporated into the cage of UiO-66 by coordinating to Zr^{4+} in a manner similar to the "ship-in-a-bottle". This method can circumvent the size and geometry limitation of cages of MOFs and meanwhile avoid the leaching of Fe-TCPP [39]. Fourier-transform infrared (FTIR) spectra of tetradecanoic acid and Fe^{3+}@UiO-66-C_{14} show that the peak at 1701.7 cm^{-1} ascribed to the –COOH group in tetradecanoic acid shifts to 1704.3 cm^{-1} in Fe^{3+}@UiO-66-C_{14} (Fig. S3 online). This shift supports the coordination of tetradecanoic acid and Zr^{4+}. Scanning electron microscopy (SEM) and transmission electron microscopy (TEM) images indicate the presence of octahedral nanocrystals in the MOFs (Fig. 1a, b). The Fe contents in all Fe^{3+}@UiO-66-C_n are determined to be approximately 0.8% using inductively coupled plasma atomic emission spectroscopy (ICP-AES) (Table S1 online). FTIR spectra for the samples that introduced long-chain saturated fatty acids show three additional peaks at 2852, 2923, and 2957 cm^{-1} assignable to the aliphatic C–H stretching vibrations (2852 and 2923 cm^{-1} for CH_2 and 2957 cm^{-1} for CH_3) (Fig. S4 online) [40–42], indicating the successful incorporation of the alkyl chains to the MOFs. Furthermore, the diffuse reflectance infrared Fourier-transform (DRIFT) spectra show a significant decrease in the intensities of the characteristic peaks at approximately 3673 and 2769 cm^{-1}, which correspond to the chelating sites (the terminal –OH/–OH_2 and μ_3-OH groups) on the Zr-oxo upon the fatty acid modification (Fig. S5 online). This observation further supports the successful anchoring of fatty acids to the Zr-oxo cluster [41,43]. The approximate amount of modified monocarboxylic acids, is estimated to be comparable in all Fe^{3+}@-UiO-66-C_n catalysts based on thermogravimetric analyses (Fig. S6 online), despite the challenges in precise quantification. Water contact angles have been measured to assess the hydrophobicity of the samples. The contact angles of the pristine MOF and Fe^{3+}@-UiO-66 are approximately 5°, which increase to 117.5°, 120.9°, 123.6°, and 131.1° upon introducing fatty acids with C_{12}, C_{14}, C_{16}, and C_{18} chain, respectively (Fig. 1c), demonstrating that the intro-

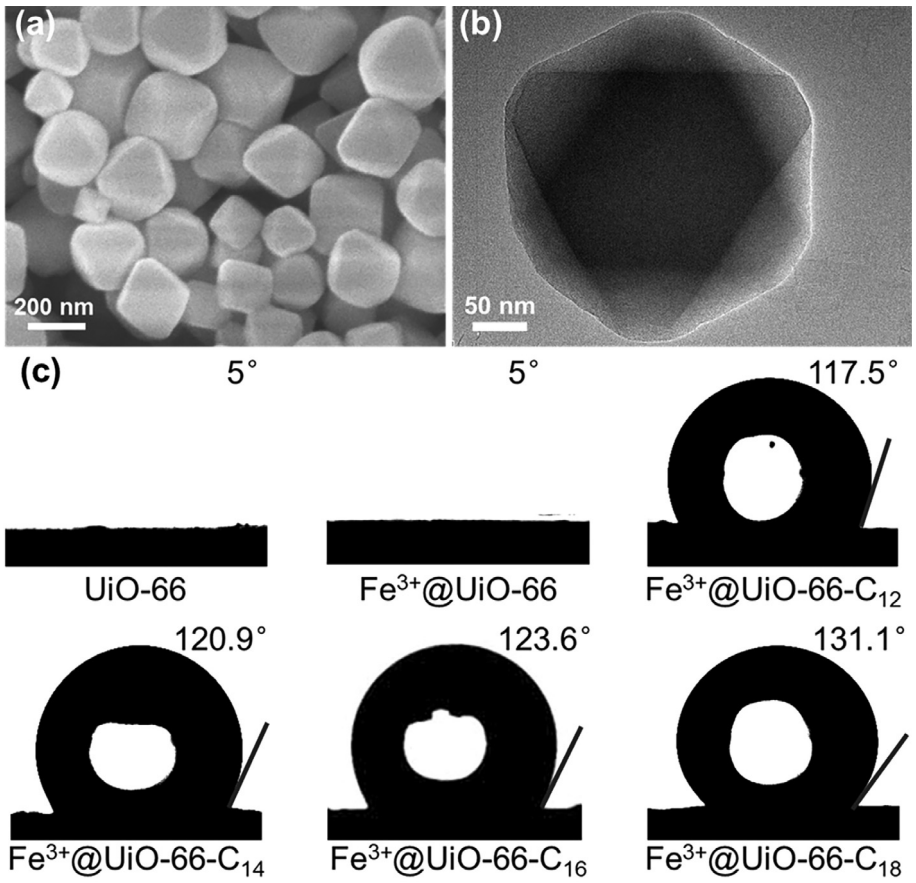

Fig. 1. SEM (a) and TEM (b) images for Fe^{3+}@UiO-66-C_{14}. (c) Static water contact angles of UiO-66, Fe^{3+}@UiO-66 and Fe^{3+}@UiO-66-C_n (n = 12, 14, 16, and 18).

duction of long-chain alkyl acids converts the MOF from hydrophilic to hydrophobic. The product obtained by replacing tetradecanoic acid with methyl tetradecate, in which the carboxylic group is blocked, shows a hydrophilic feature, suggesting that the coordination between tetradecanoic acid and Zr^{4+} is responsible for the successful introduction of fatty acids into Fe^{3+}@UiO-66-C_n catalysts (Fig. S7 online). The Brunauer-Emmett-Teller (BET) surface area measured by N_2 sorption isotherms gradually decreases from 1060 to 647 $m^2\ g^{-1}$ (with pore size distributions mostly in the range of 6.5–15 Å) as the chain length of alkyl acids increases (Fig. S8 online). This decrease is possibly due to the mass and pore occupation by the introduced alkyl acids.

X-ray photoelectron spectroscopy (XPS) was employed to analyze the chemical state of the Fe species in these catalysts. The XPS spectrum of Fe^{3+}@UiO-66 confirms the presence of Fe species in the +3 oxidation states, as evidenced by the Fe $2p_{3/2}$ binding energy at 711.00 eV (Fig. S9 online) [42,44]. The introduction of long-chain alkyl acids causes the Fe $2p_{3/2}$ peak shifts to lower binding energies. This shift is observed to gradually decrease with the increase of the chain length (Fig. S9 online), which implies an increased electron density of Fe after introducing alkyl acids. This phenomenon could be ascribed to the enhanced electron-donating effect with the increase of the alkyl chains in the fatty acids attached to the Zr-oxo clusters of UiO-66, which successively leads to varied electron transfer from long-chain alkyl acids to Fe through Zr-oxo clusters. To further investigate the Fe electronic state in the catalysts, carbon monoxide (CO) adsorption analysis using DRIFT spectroscopy is performed. As depicted in Fig. 2a, the stretching band of CO on Fe^{3+}@UiO-66 is located in 1955 cm^{-1}, which is red-shifted compared to free CO (2143 cm^{-1}). Although of small magnitudes, a further red-shift trend is observed after introducing long-chain alkyl acids, in which the trend continues gradually as the chain length increases in Fe^{3+}@UiO-66-C_n. The red-shift of CO is usually ascribed to the Fe $d_\pi \rightarrow$ CO π^* back-donation that weakens the C–O bond in comparison to free CO [45]. The observed increasing red shifts, therefore, suggest an enhanced π back-donation effect, consistent with an increased d electron density of Fe in Fe^{3+}@UiO-66-C_n with increased alkyl chain lengths. Moreover, the Fe K-edge X-ray absorption near-edge structure (XANES) spectra indicate that the absorption edge of Fe^{3+}@UiO-66-C_{14} shifts to a lower energy side compared to Fe^{3+}@UiO-66, manifesting the lower oxidation state of Fe sites in the former, which is in line with the observed XPS results (Fig. 2b and Fig. S10 online).

3.2. Catalytic activity

Given the similarity between Fe-TCPP with Fe^{3+} sites and sMMO, we initially examined the catalytic performance of Fe-TCPP for the CH_4 oxidation using H_2O_2 as the oxidant at 50 °C. Consistent with expectations, Fe-TCPP is able to convert CH_4 to CH_3OH, despite that the conversion and selectivity to CH_3OH are very low (Fig. 3 and Fig. S11 online). The poor performance may be attributed to the formation of the bridged μ-oxide dimers occurred in the Fe-TCPP catalyst [46,47]. To our delight, compared to Fe-TCPP, Fe^{3+}@UiO-66 shows a much better CH_3OH yield (2.95 vs. 0.07 μmol) and selectivity (15.4% vs. 2.9%) in the CH_4 oxidation (Fig. 3). The significantly improved performance highlights that UiO-66 as a support plays a critical role in converting CH_4 to CH_3OH. Anchoring dodecylic (C_{12}) acid to the MOF leads to a further enhancement in CH_3OH selectivity to 27.3% (76.1% among all liquid oxygenate products). Remarkably, the CH_3OH selectivity continuously

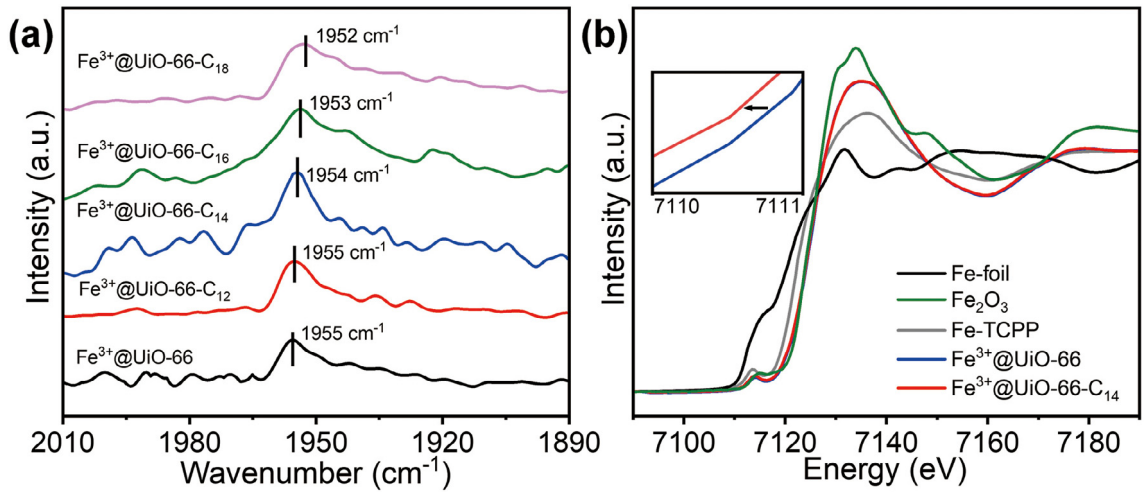

Fig. 2. (Color online) (a) DRIFT spectra of CO adsorbed on Fe^{3+}@UiO-66 and Fe^{3+}@UiO-66-C_n (n = 12, 14, 16, and 18) after being purged with Ar for 30 min. (b) The Fe K-edge XANES spectra for Fe foil, Fe-TCPP, Fe_2O_3, Fe^{3+}@UiO-66, and Fe^{3+}@UiO-66-C_{14}.

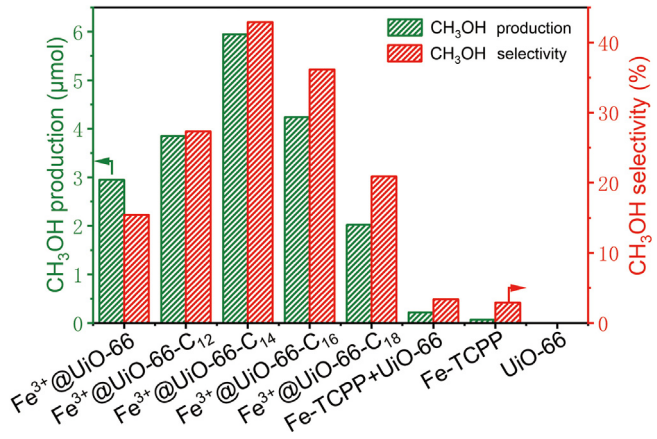

Fig. 3. (Color online) Catalytic performance of Fe^{3+}@UiO-66, Fe^{3+}@UiO-66-C_n (n = 12, 14, 16, and 18), Fe-TCPP, UiO-66, and Fe-TCPP + UiO-66 for CH_4 oxidation (reaction conditions: catalyst 27 mg, CH_4 pressure 30 bar, H_2O_2 0.5 mol L^{-1} (aq), 50 °C, reaction time 30 min).

increases and reaches a maximum of 42.9% (77.0% among all liquid products) when tetradecanoic (C_{14}) acid is furnished onto the MOF. Subsequently, the selectivity of CH_3OH decreases to 36.2% and 20.9% with the further increase of the chain lengths to palmitic (C_{16}) acid and stearic (C_{18}) acid, respectively. Overall, as the chain length of the alkyl acids increases, the CH_3OH selectivity exhibits a volcano-type trend (Fig. 3). Under the optimal conditions, a normalized activity of 55.8 mmol g_{Fe}^{-1} h^{-1} with a selectivity of 42.9% for CH_3OH has been realized by Fe^{3+}@UiO-66-C_{14}, which is a catalyst based on the earth-abundant element of Fe. The overall performance of Fe^{3+}@UiO-66-C_{14} surpasses that of some state-of-art catalysts in CH_4 oxidation [3,20,48], and is even comparable to the catalysts that use noble metals (Table S4 online) [1,38,49]. Taken together, the aforementioned results demonstrate that the activity and CH_3OH selectivity in the CH_4 conversion are effectively regulated by the hydrophobic microenvironment of the Fe-TCPP sites created by the long-chain alkyl acids with varying chain lengths.

To determine the carbon source in the products, we have conducted an isotope labeling experiment using $^{13}CH_4$ as the reactant. The products of $^{13}CH_4$ oxidation over Fe^{3+}@UiO-66-C_{14} have been analyzed using the synchrotron radiation photoionization mass spectrometry (SR-PIMS) at a photon energy of 11.8 eV. The spectrum shows signals at m/z = 33 and 47, which are assignable to ^{13}-CH_3OH and $H^{13}COOH$, respectively (Fig. 4a and Fig. S11 online), confirming that CH_3OH is indeed produced through the oxidation of CH_4. The peaks of formaldehyde (HCHO), which is considered to be an overoxidation product of CH_3OH, are also observed at m/z = 31 or 30 when $^{13}CH_4$ or $^{12}CH_4$ is used, respectively (Fig. 4a) [50]. As an intermediate, the concentration of HCHO in the reaction system is low because of its rapid oxidation into HCOOH and CO_2. Additionally, the overlap of its chemical shift with H_2O makes its detection challenging by ^{1}H nuclear magnetic resonance (NMR). However, here, SR-PIMS allows a convincing identification of the existence of HCHO. The signal of HCHO is intensified when CH_3OH is used (Fig. 4a and Fig. S12 online). The product HCOOH can be detected regardless of whether CH_3OH or HCHO is used as the reactant (Figs. S13, S14 online). The *operando* SR-PIMS results indicate that HCHO appears at the early stage of CH_4 oxidation, whereas the signal of HCOOH does not appear until 20 min after the oxidation (Fig. S15 online). Therefore, it is very likely that CH_4 is initially oxidized to CH_3OH and CH_3OOH, which are further converted to HCHO and HCOOH.

Recycling experiments demonstrate that Fe^{3+}@UiO-66-C_{14} exhibited no noticeable activity or selectivity loss during the three consecutive runs (Fig. 4b). Furthermore, powder XRD patterns manifest that the crystallinity of Fe^{3+}@UiO-66-C_{14} remains after the catalysis and no additional peaks can be observed (Fig. S16 online). The N_2 sorption isotherm of Fe^{3+}@UiO-66-C_{14} after the reaction shows the preserved porous nature of the MOF after the reaction (Fig. S17 online). FTIR and ^{1}H NMR spectra of Fe^{3+}@UiO-66-C_{14} before and after the reaction exhibit minimal differences, demonstrating that the organic components of the catalysts are stable during the reaction (Figs. S18, S19 online). The preference of oxidation on C–H bond of methane rather than on C–C and C–O bonds of the catalyst may be attributed to the spatial segregation and polarity mismatch between the C–O/C–H bonds and Fe sites [51]. Meanwhile, the Fe content in the catalyst is also maintained as confirmed by the ICP-AES results (Table S2 online). XPS data confirmed the persistence of the +3 oxidation state of Fe after the catalytic test (Fig. S20 online). Contact angle analysis of the catalyst Fe^{3+}@UiO-66-C_{14} after the reaction suggests that its hydrophobic nature remains after the catalytic test (Fig. S21 online). These findings collectively demonstrate the excellent stability of the Fe^{3+}@UiO-66-C_{14} catalyst, possibly attributed to

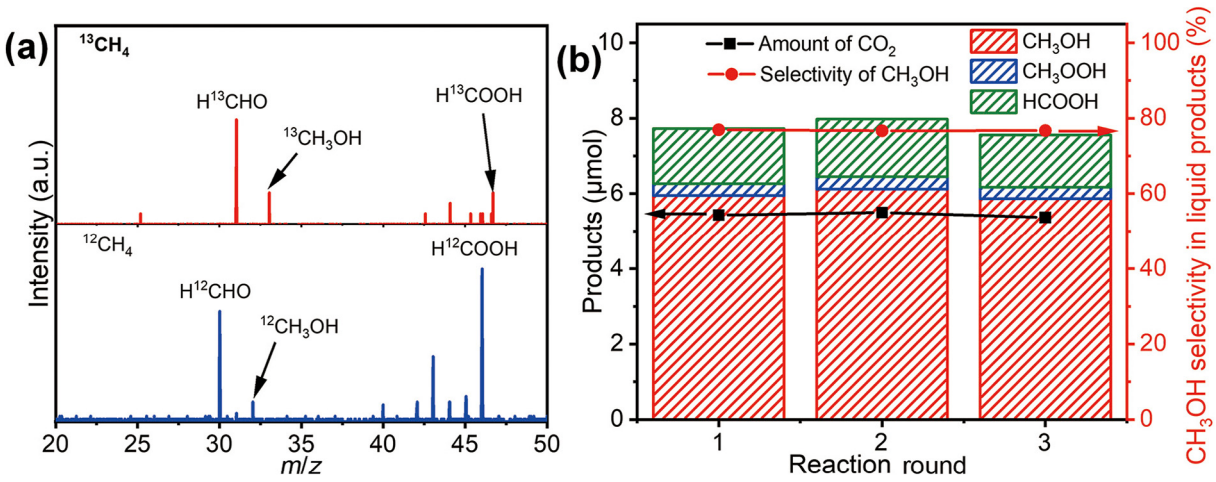

Fig. 4. (Color online) (a) Photoionization mass spectra of the products in the $^{13}CH_4$ and $^{12}CH_4$ oxidation reactions over Fe^{3+}@UiO-66-C_{14} with H_2O_2 as the oxidant at a photon energy of 11.8 eV, and (b) recycling performance of Fe^{3+}@UiO-66-C_{14} in the CH_4 oxidation.

the robust MOF skeleton that effectively prevents the leaching and dimerization of the hosted active Fe-TCPP units.

3.3. Mechanism study

Given the widely accepted notion that CH_4 adsorption and activation on the catalyst play a crucial role in initiating the oxidation of CH_4 [50], we have performed temperature-programmed desorption mass spectrometric analysis (TPD-MS) with CH_4 as feed gas to study the adsorption of CH_4 on the surface of different catalysts. The results suggest that the desorption temperatures of CH_4 from Fe^{3+}@UiO-66 are approximately 129 and 278 °C, which can be assigned to different CH_4 consumption processes. These two temperatures rise to 144 and 292 °C, respectively, for Fe^{3+}@UiO-66-C_{14} (Fig. 5a). Meanwhile, the CH_4 uptake of Fe^{3+}@UiO-66-C_{14} is 11.1 $cm^3\ g^{-1}$ at 1 bar (1 bar = 100 kPa) and 298 K, higher than the 8.1 $cm^3\ g^{-1}$ for Fe^{3+}@UiO-66 (Fig. S22 online). Both results jointly support that the incorporation of the alkyl acids improves CH_4 adsorption. Since the CH_4 and CH_3OH oxidations compete for the Fe active sites, the enhanced CH_4 adsorption is expected to reduce the relative concentration of CH_3OH around the Fe sites, thereby suppressing the CH_3OH overoxidation and promoting higher selectivity to CH_3OH [50]. This assumption agrees with the experimental results: the overoxidized products (HCOOH and CO_2) obtained by Fe^{3+}@UiO-66 account for 78.9% of all the CH_4 oxidation products, whereas the corresponding overoxidized products over Fe^{3+}@UiO-66-C_{14} are reduced to 52.4%.

To further examine the activation of CH_4 adsorbed on the catalyst, near-ambient pressure XPS (NAP-XPS) has been carried out on Fe^{3+}@UiO-66-C_{14} (Fig. 5b). Two peaks at 284.8 and 288.8 eV that are assigned to the C=C, C–C, C–H, and C=O bands of the organic linker (BDC) and tetradecanoic acid in the catalyst are observed on the C 1s spectra [52,53]. There is no additional peak observed after exposing the sample to 1 mbar of CH_4 at 300 K, which may be due to the overlapping between the CH_4 signals and those noted above. Upon increasing the temperature to 450 K, a new peak at 285.5 eV can be observed, which is identified as the characteristic peak of $*CH_x$ (including $\cdot CH_3$, $\cdot CH_2$, and $\cdot CH$) species. This result implies that CH_4 undergoes activation on the surface of the catalyst, consistent with the literature reports [2,54,55]. Additionally, the formation of $\cdot CH_3$ from the attack of CH_4 by reactive oxygen species generated by H_2O_2 may also contribute to the activation of CH_4 in the actual catalytic reactions [56–58]. *In situ* diffuse reflectance infrared Fourier transform (DRIFTS) has been adopted to identify the intermediate species on different catalysts. Two peaks at 1305 and 3015 cm^{-1} appear upon exposing the catalyst to a CH_4 atmosphere for 30 min, which can be recognized as the characteristic peaks of absorbed CH_4 (Fig. S23 online) [56,59–61]. These peaks are assigned to $*CO_3^{2-}$ (1745 cm^{-1}), *CO (1823 and 1952 cm^{-1}), and $*CH_3O$ (2856 cm^{-1}), providing evidence for the conversion of CH_4 to oxygenated species on the catalyst (Fig. 5c) [59–62]. In comparison to Fe^{3+}@UiO-66, Fe^{3+}@UiO-66-C_{14} exhibits an increased peak intensity of the $*CH_3O$ intermediate while the intensities of $*CO_3^{2-}$ and *CO decrease. This observation aligns with the enhanced CH_3OH selectivity of Fe^{3+}@UiO-66-C_{14}. In the reaction, the Fe site has several roles. Our above results show that CH_4 is first adsorbed on the Fe site, then activated to form $*CH_x$, and further oxidated to $*CH_3O$, $*CO_3^{2-}$, *CO, and other adsorbed species. After the reaction, these adsorbed species will be released from the Fe site to form the products. In this context, the electronic state of Fe sites will have a strong effect on interactions between the Fe site, CH_4, and intermediate species, thereby influencing the activation of CH_4 and the desorption of products.

In addition to $\cdot CH_x$, reactive oxygen species, such as superoxide anion radical ($O_2^{\cdot-}$) or hydroxyl radical ($\cdot OH$) generated from H_2O_2, are also important intermediates involved in CH_4 oxidation. To probe the specific reactive oxygen species in the reaction, electron paramagnetic resonance (EPR) experiments employing 5,5-dimethyl-pyrroline-*N*-oxide (DMPO) as a radical trapping agent have been conducted. The EPR spectrum of the reaction mixture using Fe^{3+}@UiO-66 exhibits a characteristic signal of DMPO-$\cdot OH$ (Fig. 5d), providing evidence that $\cdot OH$ is the main reactive oxygen species in the reaction. No DMPO-$CH_3\cdot$ peaks can be observed possibly due to the rapid combination of $\cdot CH_3$ with the abundant $\cdot OH$ [18,19]. In comparison to Fe^{3+}@UiO-66, the signal intensity of DMPO-$\cdot OH$ generated by Fe^{3+}@UiO-66-C_{14} is much weaker, indicating that the concentration of $\cdot OH$ in the reaction solution is greatly reduced upon introducing tetradecanoic acid. Since the $\cdot OH$ concentration is likely associated with the effective H_2O_2 concentration around Fe cites, we have conducted a decomposition test of H_2O_2 to estimate the accessibility of H_2O_2 to Fe active sites in Fe^{3+}@UiO-66 and Fe^{3+}@UiO-66-C_n. The results manifest that the decomposition rate gradually decreases for the catalysts with increased chain lengths of the alkyl acids (Fig. S24 online). Increasing the chain length results in the enhanced hydrophobicity of the catalyst, thereby impeding the diffusion of the hydrophilic H_2O_2 through the hydrophobic shell to access Fe active sites. In this scenario, the long-chain alkyl acids behave as "molecular-fence", con-

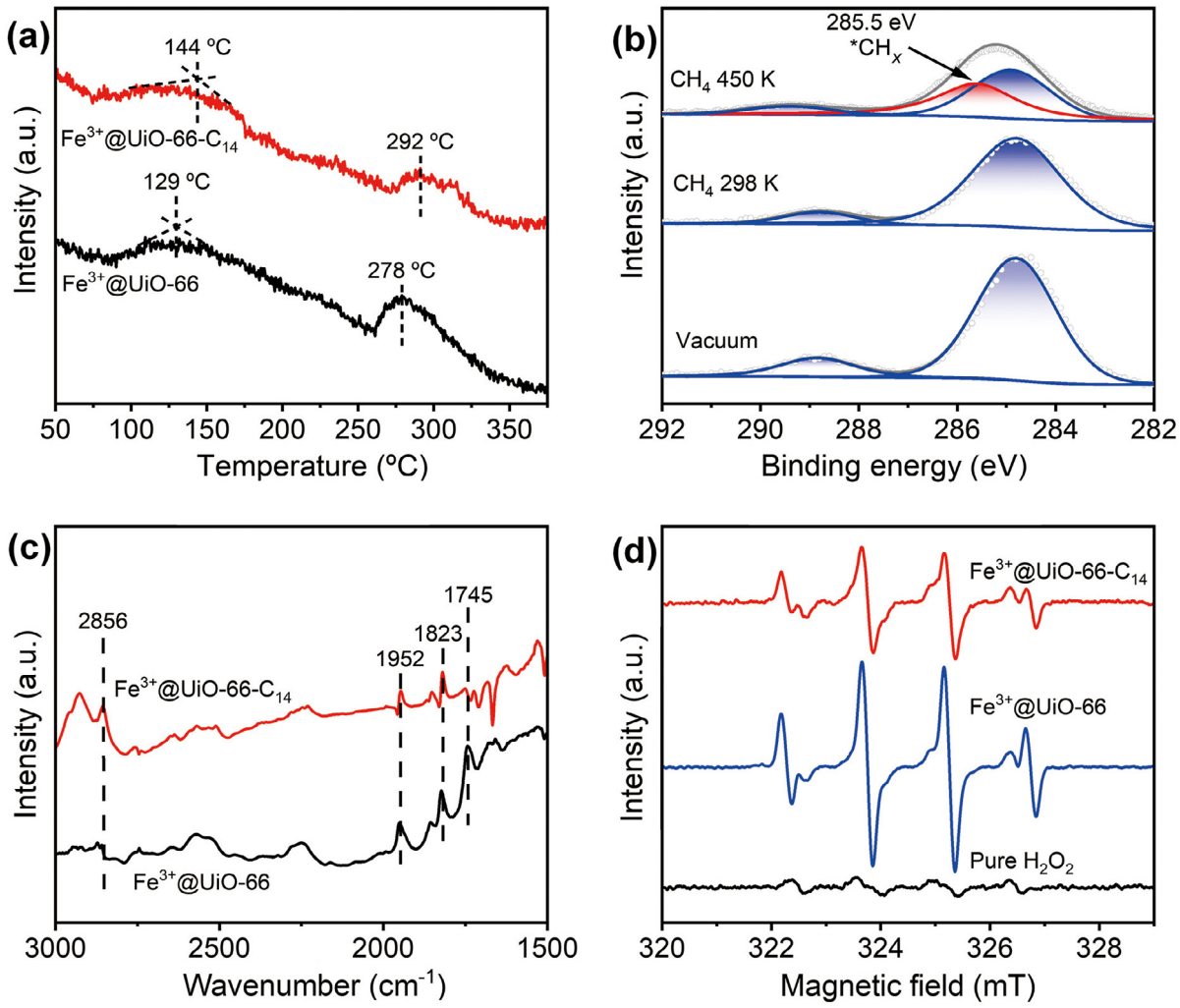

Fig. 5. (Color online) (a) TPD-MS profiles (m/z = 16) of CH_4 on the Fe^{3+}@UiO-66 and Fe^{3+}@UiO-66-C_{14}. (b) The C 1s XPS spectra of Fe^{3+}@UiO-66-C_{14} measured in ultrahigh vacuum and after introducing 1 mbar of CH_4 at different temperatures. (c) DRIFT spectra of CH_4 adsorbed on Fe^{3+}@UiO-66 and Fe^{3+}@UiO-66-C_{14} after purging with Ar gas for 30 min. Species appear when the physically adsorbed CH_4 is removed by Ar flushing (bubbling through H_2O_2 solution). (d) EPR detection of ·OH generation over Fe^{3+}@UiO-66 and Fe^{3+}@UiO-66-C_{14} with H_2O_2 as the oxidant and DMPO as the radical trapping agent.

trolling the H_2O_2 concentration around the Fe sites [1]. Thus, the amount of H_2O_2 trapped by the catalysts gradually decreases with increasing chain length of the alkyl acids, supporting the gating effect of the fatty acids to H_2O_2 diffusion (Table S3 online). In the reaction, H_2O_2 participates not only in CH_4 to CH_3OH transformation but also in CH_3OH to HCOOH or CO_2 conversions. Thus the amount of H_2O_2 around the Fe sites should be controlled to a suitable level to promote the CH_4 to CH_3OH path, meanwhile suppresses CH_3OH to HCOOH or CO_2 path. Considering that the ·OH generated from H_2O_2 is involved in both the formation and overoxidation of CH_3OH, Fe^{3+}@UiO-66-C_{14}, with its moderate hydrophobicity, has the potential to keep an optimal amount of ·OH around the Fe sites among all catalysts, thus giving rise to the highest CH_3OH selectivity.

4. Conclusion

In summary, Fe(III) porphyrin is incorporated into a MOF dangling with alkyl acids bearing different chain lengths, affording a catalytic platform inspired by the structure of sMMO, namely Fe^{3+}@UiO-66-C_n. The resulting catalysts demonstrate remarkable selectivity in CH_4 oxidation to CH_3OH at near room temperature with the aid of H_2O_2. Importantly, the long-chain fatty acids anchored to UiO-66 provide an effective means to fine-tune the CH_3OH selectivity by modulating the electronic state of Fe active sites, improving CH_4 adsorption and restricting the amount of H_2O_2 around the Fe sites, akin to the microenvironment modulation mechanism found in sMMO. With proper hydrophobic modulation, the catalyst Fe^{3+}@UiO-66-C_{14} maintains optimal H_2O_2 encompassment and ·OH concentration around Fe sites, effectively mitigating the overoxidation of CH_3OH and thereby leading to the highest CH_3OH selectivity among Fe^{3+}@UiO-66-C_n catalysts. This work serves as a vivid and unprecedented illustration of the rational fabrication of bioinspired catalysts, wherein the microenvironment of catalytic sites is finely tuned through the utilization of MOFs as a multifunctional platform.

Conflict of interest

The authors declare that they have no conflict of interest.

Acknowledgments

This work was supported by the National Key Research and Development Program of China (2021YFA1500402), the Strategic Priority Research Program of the Chinese Academy of Sciences

(CAS) (XDB0450302), the National Natural Science Foundation of China (22161142001, U22A20401, and 22101269), International Partnership Program of CAS (123GJHZ2022028MI), and the Fundamental Research Funds for the Central Universities (WK3450000007 and WK2060000038). The authors acknowledge the XAS supports from Beijing Synchrotron Radiation Facility (BSRF).

Author contributions

Jianfei Sui and Ming-Liang Gao performed the experiments and wrote the manuscript; Bing Qian, Chengyuan Liu, and Yang Pan preformed the SR-PIMS experiments; Zheng Meng discussed the results and contributed to the scientific interpretation and editing of the manuscript; Daqiang Yuan preformed the CH_4 uptake experiments; Hai-Long Jiang led the project and supervised the research. All authors discussed the results and commented on the manuscript.

Appendix A. Supplementary materials

Supplementary materials to this article can be found online at https://doi.org/10.1016/j.scib.2023.07.031.

References

[1] Jin Z, Wang L, Zuidema E, et al. Hydrophobic zeolite modification for *in situ* peroxide formation in methane oxidation to methanol. Science 2020;367:193–7.
[2] Liu Z, Huang E, Orozco I, et al. Water-promoted interfacial pathways in methane oxidation to methanol on a CeO_2-Cu_2O catalyst. Science 2020;368:513–7.
[3] Meng X, Cui X, Rajan NP, et al. Direct methane conversion under mild condition by thermo-, electro-, or photocatalysis. Chem 2019;5:2296–325.
[4] Song H, Meng X, Wang ZJ, et al. Solar-energy-mediated methane conversion. Joule 2019;3:1606–36.
[5] Wu B, Lin T, Huang M, et al. Tandem catalysis for selective oxidation of methane to oxygenates using oxygen over PdCu/zeolite. Angew Chem Int Edit 2022;61:e202204116.
[6] Tomkins P, Ranocchiari M, van Bokhoven JA. Direct conversion of methane to methanol under mild conditions over cu-zeolites and beyond. Acc Chem Res 2017;50:418–25.
[7] Schulz CE, Castillo RG, Pantazis DA, et al. Structure-spectroscopy correlations for intermediate q of soluble methane monooxygenase: insights from QM/MM calculations. J Am Chem Soc 2021;143:6560–77.
[8] Wang VC, Maji S, Chen PP, et al. Alkane oxidation: methane monooxygenases, related enzymes, and their biomimetics. Chem Rev 2017;117:8574–621.
[9] Koo CW, Rosenzweig AC. Biochemistry of aerobic biological methane oxidation. Chem Soc Rev 2021;50:3424–36.
[10] Kodera M, Kawahara Y, HitomiY, et al. Reversible O–O bond scission of peroxodiiron(III) to high-spin oxodiiron(IV) in dioxygen activation of a diiron center with a bis-tpa dinucleating ligand as a soluble methane monooxygenase model. J Am Chem Soc 2012;134:13236–9.
[11] Honarmand EK, Hagedoorn PL, Hagen WR, et al. Unity in the biochemistry of the iron-storage proteins ferritin and bacterioferritin. Chem Rev 2015;115:295–326.
[12] Dinh KT, Sullivan MM, Serna P, et al. Viewpoint on the partial oxidation of methane to methanol using Cu- and Fe-exchanged zeolites. ACS Catal 2018;8:8306–13.
[13] Song WJ, Gucinski G, Sazinsky MH, et al. Tracking a defined route for O_2 migration in a dioxygen-activating diiron enzyme. Proc Natl Acad Sci USA 2011;108:14795–800.
[14] Srinivas V, Banerjee R, Lebrette H, et al. High-resolution XFEL structure of the soluble methane monooxygenase hydroxylase complex with its regulatory component at ambient temperature in two oxidation states. J Am Chem Soc 2020;142:14249–66.
[15] Kim H, An S, Park YR, et al. MMOD-induced structural changes of hydroxylase in soluble methane monooxygenase. Sci Adv 2019;5:eaax0059.
[16] Baik MH, Newcomb M, Friesner RA, et al. Mechanistic studies on the hydroxylation of methane by methane monooxygenase. Chem Rev 2003;103:2385–419.
[17] Yu T, Li Z, Jones W, et al. Identifying key mononuclear Fe species for low-temperature methane oxidation. Chem Sci 2021;12:3152–60.
[18] Zhao W, Shi Y, Jiang Y, et al. Fe-O clusters anchored on nodes of metal–organic frameworks for direct methane oxidation. Angew Chem Int Edit 2021;60:5811–5.
[19] Cui X, Li H, Wang Y, et al. Room-temperature methane conversion by graphene-confined single iron atoms. Chem 2018;4:1902–10.
[20] Yu T, Li Z, Lin L, et al. Highly selective oxidation of methane into methanol over Cu-promoted monomeric Fe/ZSM-5. ACS Catal 2021;11:6684–91.
[21] Vitillo JG, Bhan A, Cramer CJ, et al. Quantum chemical characterization of structural single Fe(II) sites in MIL-type metal-organic frameworks for the oxidation of methane to methanol and ethane to ethanol. ACS Catal 2019;9:2870–9.
[22] Snyder BER, Bols ML, Schoonheydt RA, et al. Iron and copper active sites in zeolites and their correlation to metalloenzymes. Chem Rev 2018;118:2718–68.
[23] Zhou HC, Kitagawa S. Metal–organic frameworks (MOFs). Chem Soc Rev 2014;43:5415–8.
[24] Furukawa H, Cordova KE, O'Keeffe M, et al. The chemistry and applications of metal-organic frameworks. Science 2013;341:1230444.
[25] Islamoglu T, Goswami S, Li Z, et al. Postsynthetic tuning of metal-organic frameworks for targeted applications. Acc Chem Res 2017;50:805–13.
[26] Jiao L, Seow JYR, Skinner WS, et al. Metal–organic frameworks: structures and functional applications. Mater Today 2019;27:43–68.
[27] Li B, Wen HM, Cui Y, et al. Emerging multifunctional metal–organic framework materials. Adv Mater 2016;28:8819–60.
[28] Luo YH, Dong LZ, Liu J, et al. From molecular metal complex to metal–organic framework: the CO_2 reduction photocatalysts with clear and tunable structure. Coord Chem Rev 2019;390:86–126.
[29] Zhang H, Nai J, Yu L, et al. Metal–organic framework-based materials as platforms for renewable energy and environmental applications. Joule 2017;1:77–107.
[30] Wei YS, Zou L, Wang HF, et al. Micro/nano-scaled metal-organic frameworks and their derivatives for energy applications. Adv Energy Mater 2021;12:2003970.
[31] Chen Y, Ma S. Biomimetic catalysis of metal-organic frameworks. Dalton Trans 2016;45:9744–53.
[32] Wright AM, Wu Z, Zhang G, et al. A structural mimic of carbonic anhydrase in a metal–organic framework. Chem 2018;4:2894–901.
[33] Chen K, Wu CD. Designed fabrication of biomimetic metal–organic frameworks for catalytic applications. Coord Chem Rev 2019;378:445–65.
[34] Liang W, Wied P, Carraro F, et al. Metal–organic framework-based enzyme biocomposites. Chem Rev 2021;121:1077–129.
[35] Jiao L, Wang J, Jiang HL. Microenvironment modulation in metal–organic framework-based catalysis. Acc Mater Res 2021;2:327–39.
[36] Quesne MG, Senthilnathan D, Singh D, et al. Origin of the enhanced reactivity of μ-nitrido-bridged diiron(IV)-oxo porphyrinoid complexes over cytochrome p450 compound I. ACS Catal 2016;6:2230–43.
[37] Khade RL, Zhang Y. Catalytic and biocatalytic iron porphyrin carbene formation: effects of binding mode, carbene substituent, porphyrin substituent, and protein axial ligand. J Am Chem Soc 2015;137:7560–3.
[38] Ab Rahim MH, Forde MM, Jenkins RL, et al. Oxidation of methane to methanol with hydrogen peroxide using supported gold-palladium alloy nanoparticles. Angew Chem Int Edit 2013;52:1280–4.
[39] Sun Y, Sun L, Feng D, et al. An *in situ* one-pot synthetic approach towards multivariate zirconium MOFs. Angew Chem Int Edit 2016;55:6471–5.
[40] Wang M, Zhang Z, Zhong H, et al. Surface-modified phthalocyanine-based two-dimensional conjugated metal–organic framework films for polarity-selective chemiresistive sensing. Angew Chem Int Edit 2021;60:18666–72.
[41] Ma X, Liu H, Yang W, et al. Modulating coordination environment of single-atom catalysts and their proximity to photosensitive units for boosting MOF photocatalysis. J Am Chem Soc 2021;143:12220–9.
[42] Xu C, Pan Y, Wan G, et al. Turning on visible-light photocatalytic C–H oxidation over metal–organic frameworks by introducing metal-to-cluster charge transfer. J Am Chem Soc 2019;141:19110–7.
[43] Sui J, Liu H, Hu S, et al. A general strategy to immobilize single-atom catalysts in metal–organic frameworks for enhanced photocatalysis. Adv Mater 2022;34:e2109203.
[44] Jiao L, Zhang R, Wan G, et al. Nanocasting SiO_2 into metal-organic frameworks imparts dual protection to high-loading Fe single-atom electrocatalysts. Nat Commun 2020;11:2831.
[45] Bloch ED, Hudson MR, Mason JA, et al. Reversible CO binding enables tunable CO/H_2 and CO/N_2 separations in metal-organic frameworks with exposed divalent metal cations. J Am Chem Soc 2014;136:10752–61.
[46] Li L, Yang Q, Chen S, et al. Boosting selective oxidation of cyclohexane over a metal–organic framework by hydrophobicity engineering of pore walls. Chem Commun 2017;53:10026–9.
[47] Malko D, Guo Y, Jones P, et al. Heterogeneous iron containing carbon catalyst (Fe-N/C) for epoxidation with molecular oxygen. J Catal 2019;370:357–63.
[48] Shen Q, Cao C, Huang R, et al. Single chromium atoms supported on titanium dioxide nanoparticles for synergic catalytic methane conversion under mild conditions. Angew Chem Int Edit 2020;59:1216–9.
[49] Agarwal N, Freakley SJ, McVicker RU, et al. Aqueous Au-Pd colloids catalyze selective CH_4 oxidation to CH_3OH with O_2 under mild conditions. Science 2017;358:223–7.
[50] Fan Y, Zhou W, Qiu X, et al. Selective photocatalytic oxidation of methane by quantum-sized bismuth vanadate. Nat Sustain 2021;4:509–15.
[51] Laudadio G, Deng Y, Wal K, et al. C(sp^3)–H functionalizations of light hydrocarbons using decatungstate photocatalysis in flow. Science 2020;369:92–6.
[52] Liu S, Wang Z, Zhou S, et al. Metal–organic-framework-derived hybrid carbon nanocages as a bifunctional electrocatalyst for oxygen reduction and evolution. Adv Mater 2017;29:1700874.

[53] Li J, Song S, Meng J, et al. 2D MOF periodontitis photodynamic ion therapy. J Am Chem Soc 2021;143:15427–39.
[54] Prats H, Gutierrez RA, Pinero JJ, et al. Room temperature methane capture and activation by Ni clusters supported on TiC(001): effects of metal-carbide interactions on the cleavage of the C–H Bond. J Am Chem Soc 2019;141:5303–13.
[55] Liu Z, Lustemberg P, Gutierrez RA, et al. *In situ* investigation of methane dry reforming on metal/ceria(111) surfaces: metal-support interactions and C–H bond activation at low temperature. Angew Chem Int Edit 2017;56:13041–6.
[56] Chen X, Li Y, Pan X, et al. Photocatalytic oxidation of methane over silver decorated zinc oxide nanocatalysts. Nat Commun 2016;7:12273.
[57] Bai S, Xu Y, Wang P, et al. Activating and converting CH_4 to CH_3OH via the $CuPdO_2$/CuO nanointerface. ACS Catal 2019;8:6938–44.
[58] Liang Z, Li T, Kim M, et al. Low-temperature activation of methane on the IrO_2(110) surface. Science 2017;356:299–303.
[59] Panagiotopoulou P, Kondarides DI. Effects of alkali additives on the physicochemical characteristics and chemisorptive properties of Pt/TiO_2 catalysts. J Catal 2008;260:141–9.
[60] Cheng G, Tan X, Song X, et al. Visible light assisted thermocatalytic reaction of CO + NO over $Pd/LaFeO_3$. Appl Catal B 2019;251:130–42.
[61] Zhu B, Thrimurthulu G, Delannoy L, et al. Evidence of Pd segregation and stabilization at edges of AuPd nano-clusters in the presence of CO: a combined DFT and DRIFTS study. J Catal 2013;308:272–81.
[62] Routray K, Zhou W, Kiely CJ, et al. Catalysis science of methanol oxidation over iron vanadate catalysts: nature of the catalytic active sites. ACS Catal 2010;1:54–66.

Jianfei Sui received his Ph.D. degree in Inorganic Chemistry from University of Science and Technology of China (USTC) in 2022 under the supervision of Prof. Hai-Long Jiang. His research focuses on the metal–organic framework-based materials for selective methane oxidation.

Zheng Meng received his Ph.D. degree at the Institute of Chemistry, Chinese Academy of Sciences under the supervision of Prof. Chuan-Feng Chen in 2016. He worked as a postdoctoral researcher with Prof. Katherine A. Mirica at Dartmouth College from 2016 to 2021. At late 2021, he started his research career at USTC. His current interest focuses on the development of new conductive framework materials and their applications in electronics, sensing, and catalysis.

Hai-Long Jiang earned his Ph.D. degree (2008) in Inorganic Chemistry from Fujian Institute of Research on the Structure of Matter, Chinese Academy of Sciences. He subsequently worked at the National Institute of Advanced Industrial Science and Technology (AIST, Japan), first as an AIST Fellow and later as a JSPS Fellow during 2008–2011. After a postdoctoral stint at Texas A&M University (USA), he became a full professor at USTC in 2013. His research interest currently lies in biomimetic microenvironment modulation (MEM) of catalytic centers based on crystalline porous materials (particularly MOFs).